

Entropy Stabilized Oxide Nanocrystals as Reaction Promoters in Lithium-O₂ Batteries

Guruprasad S. Hegde^[a] and Ramaprabhu Sundara^{*[a]}

Charge transport limitations at the Li₂O₂ discharge product-electrode interfaces hinder the rechargeability of Li–O₂ batteries. Herein, we introduce entropy stabilized oxides (ESOs) as reaction ‘promoters’ in positive electrodes that can facilitate charge transport by reducing the binding energy of the intermediates. In this work, we developed a rock-salt type entropy stabilized oxide. We show that the rock salt phase transforms into a pure, equimolar, quinary spinel on heat

treatment. A Li–O₂ battery with the developed ESOs at the positive electrode is cycled with an areal capacity of 1 mAh cm⁻² at a current rate of 0.25 mA cm⁻² to study its role as a reaction promoter. The surface, bulk, and morphological characterization are carried out for both materials. The presence of multiple cations and defects on the surface of the ESO is found to benefit the discharge product oxidation and improve the cyclic stability.

Introduction

Entropy stabilized compounds are the stable phases created because of high configurational entropy. The thermodynamics of the formation of a compound is governed by Gibbs free energy ($\Delta G = \Delta H - T\Delta S$). Negative Gibbs free energy for a reaction indicates the spontaneity of the reaction. At higher temperatures, the formation of a compound is dictated by the second term, where temperature dominates the enthalpy. In rare cases, high configurational entropy drives the formation of stable materials. Such materials are called high entropy or “entropy stabilized materials”.

The configurational entropy is maximized when the mole fractions of each component are equal. First reports on such entropy stabilization were in multicomponent alloys, where five or more elements in equal stoichiometry were employed.^[1,2] Some of these “high-entropy alloys” exhibited extraordinary structural properties. By virtue of the large number of constituent elements available, these materials offer a broad range of property tunability by substitution.^[3,4] Drawing parallel from high entropy alloys, Rost et al. demonstrated the concept of entropy stabilization in oxides for the first time.^[5] A pure rock-salt phased oxide was synthesized from heating a mixture of MgO, CoO, NiO, CuO, and ZnO at 1000 °C and quenching.

Interestingly, the constituent oxides such as MgO–ZnO and CuO–NiO, which are otherwise incompatible in a solid solution, formed a phase pure rock-salt structure in the synthesized entropy stabilized oxide (ESO). This pioneering report initiated several reports from different groups, owing to the composi-

tional flexibility and potential functional application of such oxides and similar materials. Berardan et al. explored the effect of lithium substitution in the ESO compound that Rost et al. had reported.^[6] They observed that lithium ions substituted the divalent cations with charge compensation or the creation of oxygen vacancies in the crystal. The substituted compound exhibited colossal dielectric constant. Wang et al. showed a rock salt to spinel transformation on lithium incorporation.^[7]

Structural, thermal, and magnetic properties ESOs having rock salt, spinel, perovskite phases, and different compositions have been reported thereafter.^[8–21] The class of entropy stabilized materials is being broadened, and several other entropy stabilized materials such as entropy stabilized phosphates,^[22] prussian blue analogs,^[23] nitrides,^[24] carbides,^[25] diborides,^[26–28] silicides,^[29] fluorite oxides^[30] are being explored.

Considering the flexibility in choosing the constituent elements and crystal systems, entropy stabilized materials can be used to design “tailor-made” materials for specific applications. Energy storage is one such area where such ESOs can have tremendous potential. Recently, several groups have been developing entropy stabilized materials for various energy storage applications. For example, ESOs are reported as positive, negative electrode materials and solid electrolytes for lithium-ion batteries,^[31–36] polysulfide anchoring sites in lithium-sulfur (Li–S) batteries,^[37,38] and as electrocatalysts in alkaline oxygen reduction and evolution reactions,^[39–43] CO oxidation, benzyl alcohol oxidation,^[44,45] hydroxymethyl perfural oxidation reactions.^[46]

The Li–O₂ battery is a promising contender as a high energy density future battery. Li–O₂ batteries store energy by reversibly converting Li₂O₂ into Li⁺ and O₂ during charge and discharge. Oxygen gets reduced at the cathode side of the Li–O₂ cell and reacts with Li⁺ to form Li₂O₂ during discharge. Li₂O₂ is an insulator and gets deposited as a sub-micron size toroidal discharge product on the surface of the positive electrode. Oxidation of this discharge product requires multiple steps with high overpotentials. Moreover, the increase in resistance due to Li₂O₂ deposition, contact issues with the

[a] G. S. Hegde, Prof. R. Sundara

Alternative Energy and Nanotechnology Laboratory (AENL)
Nano Functional Materials Technology Centre (NFMTC)
Department of Physics
Indian Institute of Technology Madras
CHENNAI 600036 India
E-mail: ramp@iitm.ac.in

 Supporting information for this article is available on the WWW under
<https://doi.org/10.1002/batt.202200068>

electrolyte-air interface, and degradation of cell components add further hindrances to the cell's round trip efficiency and cyclability.

Several catalyst materials are reported inspired by other aqueous metal-air battery systems during the early stages of Li–O₂ battery research. However, the oxygen reduction in aprotic electrolyte and oxidation reaction of solid and insoluble Li₂O₂ is significantly different from other aqueous metal-air batteries. There are questions on the efficacy or necessity of such catalysts in Li–O₂ batteries as the observed high overpotentials result from transport limitations rather than kinetic limitations.^[47–49] Further experiments over the catalyst efficacy suggest that materials such as nanocrystalline Co₃O₄ spinel on graphene oxide effectively reduce the overpotential in a non-conventional method. Conventional electrocatalysts lower the activation energy through electron transfer. The "promoters" in Li–O₂ batteries are believed to reduce the binding energy of the Li_{2-x}O_x intermediate and enhance its surface transport during the reaction.^[50] The effect of promoters is visible when a high amount of discharge products are available. Another effective strategy to oxidize Li₂O₂ is using redox mediators (RM) in the electrolyte.^[51] While charging, RMs get oxidized, and the oxidized RM chemically reacts with Li₂O₂. Since RMs are in the liquid state, they establish good contact with the solid discharge product enabling efficient Li₂O₂ oxidation. However, only solvated Li₂O₂ is oxidized by the RM, and shuttling of RMs to the anode can adversely affect the cell performance.^[52,53]

Considering the versatile cations present in octahedral and tetrahedral positions, entropy stabilized oxide materials can be attractive as cathode reaction promoters in Li–O₂ batteries. In the present work, we develop a new nanocrystalline spinel phased entropy stabilized oxide (ESO-S) by heat treatment of a precursor obtained by sol-gel autocombustion method (denoted as ESO-A), and study their compositional, morphological and surface features. We extend the application portfolio of entropy stabilized materials by evaluating them as cathode reaction promoters along with a LiI RM in high areal capacity Li–O₂ batteries.

Results and Discussion

Physical characterizations

Structural characterization: ESO-A is prepared by a sol-gel method where the required metal nitrate solution is mixed with citric acid to form a gel. An exothermic combustion reaction between the metal nitrates (oxidants) and citric acid (fuel) occurs when the gel is heated above 250 °C. During the combustion, metal nitrates decompose to form metal oxides, and highly reductive gases such as NH₃, CH₄, and H₂ are evolved. Niu et al.^[54] reported the formation of high entropy alloys from the reduction of these oxides by the evolved gases. The X-ray diffraction (XRD) pattern of ESO-A (Figure 1a) suggests the presence of mixed alloy-oxide phases resulting from a similar phenomenon. The broad XRD peaks indicate the formation of nanocrystals. Peaks at 35.8°, 43.8°, and 63.2° 2θ

can be indexed to (111), (002), and (022) planes of the rock salt type oxide phase and peaks at 44.9°, 51.4°, and 75.6° belong to (111), (002) and (022) planes FCC alloy phase.

A broad peak observed around 640 cm⁻¹ in the Raman spectrum could be assigned to the LO mode generally observed in rock salt type oxides.^[55] In addition, two broad peaks are observed at ~1360, ~1580 cm⁻¹, corresponding to the D and G bands of carbon. The presence of carbon D and G bands in the Raman spectra indicates the decomposition of a certain amount of citric acid leading to amorphous carbon formation.^[56] Differential scanning calorimetry (DSC) and Thermo-gravimetric analysis (TGA) of ESO-A show the decomposition of such amorphous carbon in the air around 300 °C, as shown in Figure S1(a). The amorphous carbon content was determined to be ~9%. Further decrease in weight from 450 °C to 700 °C indicates a gradual reduction and phase transformation in the sample.

A phase transformation from rock salt to a cubic Fd-3m spinel phase is observed when ESO-A is heated above 600 °C in air. The XRD patterns of ESO-A calcinated at different temperatures (Figure S2) indicate a pure spinel phase forming up to 800 °C. Minor impurity peaks appearing above 800 °C can be indexed to a rock salt structure. This second phase appearance above 800 °C is also confirmed by DSC data (Figure S1b). The reported XRD analysis of entropy stabilized spinel materials is limited only to identifying the spinel phase owing to the very small crystallite sizes.^[16,35,36,41,46] The detailed phase information cation distribution and structural elucidation of the entropy stabilized poses a significant challenge. The observed and Reitveld refined XRD patterns of ESO-S are provided in Figure 1(c). The entropy stabilized spinel phase was constructed for the refinement by considering the cubic Fe₃O₄ structure. AB₂O₄ spinels belong to this phase with the space group Fd-3 m, where A and B cations occupy 8a and 16d Wyckoff positions, respectively, and anions occupy 32e positions. The origin of the Fd-3m phase was chosen at the center of symmetry –3 m so that the fractional coordinates of 8a and 16d cationic sites are given by 1/8, 1/8, 1/8, and 1/2, 1/2, 1/2 respectively. While the transition metal cations will have different site preferences and hence different cationic distribution in the 8a and 16d sites, the distinction the same with an XRD pattern alone is extremely difficult, owing to the similar atomic scattering factors of the cations.^[57] Therefore, both Fe atoms at 8a and 16d sites were replaced by five cations (Fe, Co, Ni, Cr, Al) with equal site fractions (0.2). Both site fractions and coordinates were refined along with the unit cell parameter. All the refinement details are provided in Table S1. The unit cell parameter was found to be 0.8242 nm. Fractional coordinates were unchanged after the refinement, and minute deviations from 0.2 were observed for site fractions. Figure 1(e) represents the refined spinel phase.

Since five different cations are present in the high configurational entropy ESO-S, every adjacent cation environment in the structure is different. This local disorder will not affect the long-range order of the material and hence will not appear in the XRD spectrum. On the other hand, Raman spectroscopy is more suitable to extract information about

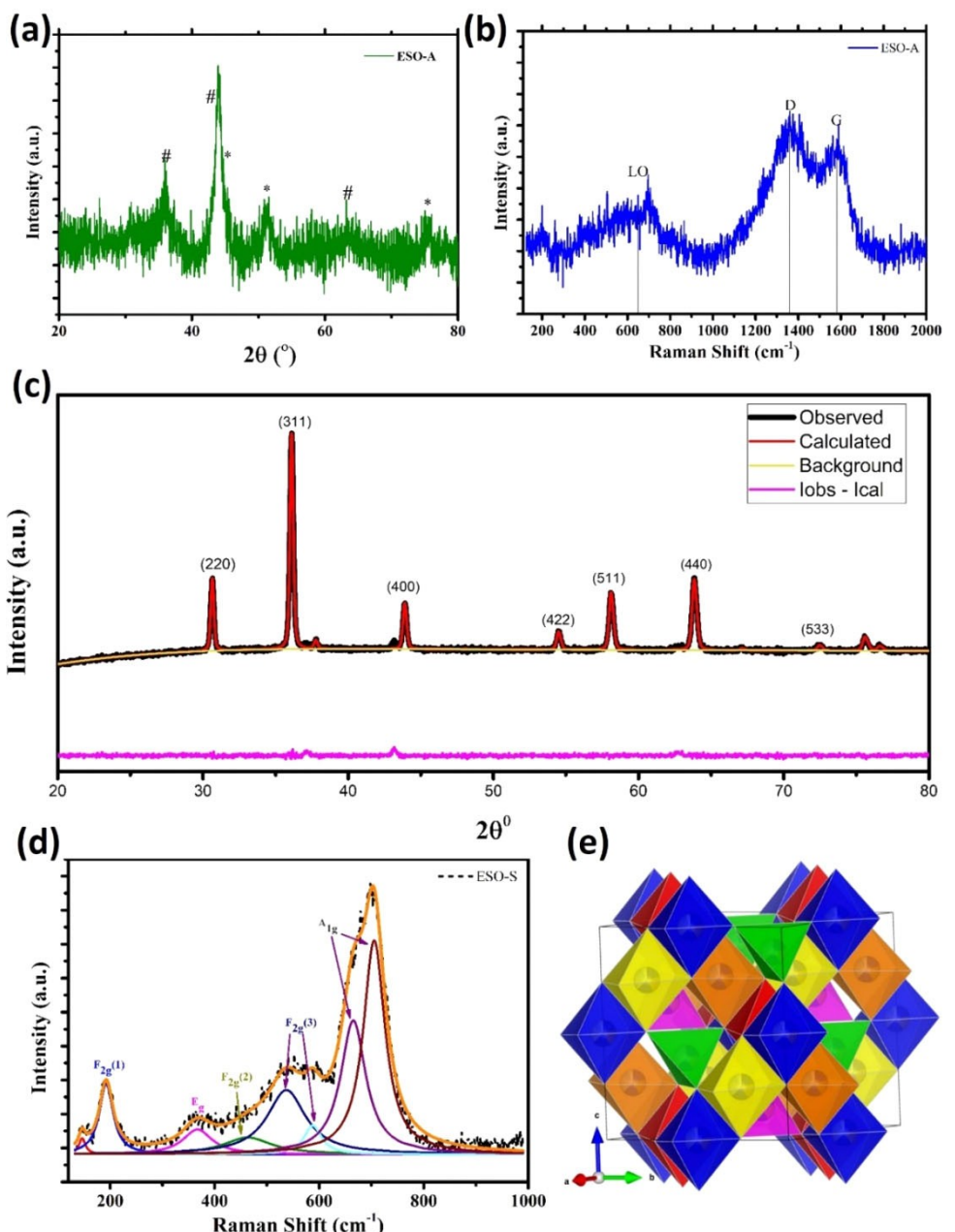


Figure 1. Structural analysis: a) X-ray diffraction pattern of ESO-A. * and # indicate FCC alloy phase and rock salt oxide phases present in ESO-A, respectively. b) Raman spectrum of ESO-A having LO mode attributed to rock salt oxide and amorphous carbon D and G bands. c) Observed XRD patterns of ESO-S along with the calculated patterns, background, and residual from Reitveld refinement. d) Observed Raman spectrum of ESO-S along with the deconvoluted Raman modes. e) Calculated structure of the ESO-S spinel with adjacent octahedral/tetrahedral positions shown in different colors to highlight the different cations present (Generated from VESTA).

such short-range disorders. Factor group analysis of an Fd-3 m normal spinel predicts five first-order Raman modes ($A_{1g} + E_g + 3F_{2g}$). The vibrational modes can depend on mass, ionic radii, and bonding forces of the different cations. Any local structural distortions caused by the substitution of other cations are observable in additional shoulder peaks. Raman spectrum of ESO-S is as shown in Figure 1(d). The observed spectrum envelope was deconvoluted using the least-square fit with a Lorentzian peak shape function. A total of eight peaks were used to fit the spectrum, including the shoulder peaks. The

highest intensity peak occurring at 705.3 cm^{-1} can be assigned to A_{1g} , corresponding to the symmetric stretching of oxygen in MO_4 tetrahedra. A shoulder peak associated with A_{1g} mode at 665.2 cm^{-1} shows the presence of multiple cations in the tetrahedral position.^[58] Similarly, peaks at 537.3 cm^{-1} and 587.9 cm^{-1} can be assigned to $F_{2g}(3)$, which is associated with the asymmetric bending of multiple MO_6 octahedra. The peak at 463.3 cm^{-1} is assigned to $F_{2g}(2)$, and at 367.3 cm^{-1} is assigned to E_g modes corresponding to asymmetric stretching of octahedra and symmetric bending of tetrahedra,

respectively. Finally, the peaks observed at 192.6 and 146.7 cm⁻¹ correspond to the F_{2g} (1) mode related to the translational motion of the whole tetrahedron.^[59] The presence

of multiple shoulder peaks indicates the local disorder created in the structure by five different cations. No trace of carbon is found in the spectrum of ESO-S.

Morphological characterization: Morphological characterization of ESO-A and ESO-S is carried out using a scanning electron microscope (SEM) and high-resolution transmission electron microscope (HRTEM) analysis. SEM images of ESO-A and ESO-S samples are shown in Figure S3(a and b), respectively. While both materials display nanocrystalline spheroidal morphology, ESO-A has much smaller particle sizes when compared to ESO-S. Particles of sizes 20–100 nm are observed in ESO-S, which form a continuous porous network. Larger particle size and formation of a network-like structure result from sintering, where smaller particles undergo densification and form larger crystallites. EDAX elemental mapping is carried out to check the homogeneity of ESO-S. It confirms that all constituent elements Co, Cr Ni, Fe, Al, and O are uniformly distributed throughout the material, as shown in Figure 2.

HRTEM images in Figure 3 provide further insights into the size distribution and morphological features of ESO-A and ESO-S nanocrystals. The ESO-A particles of sizes from 4 nm to 16 nm can be seen distributed in an amorphous carbon enclosure in Figure 3(a and b). The size distribution of the particles is shown in Figure 3(c). The individual particle sizes are calculated, and

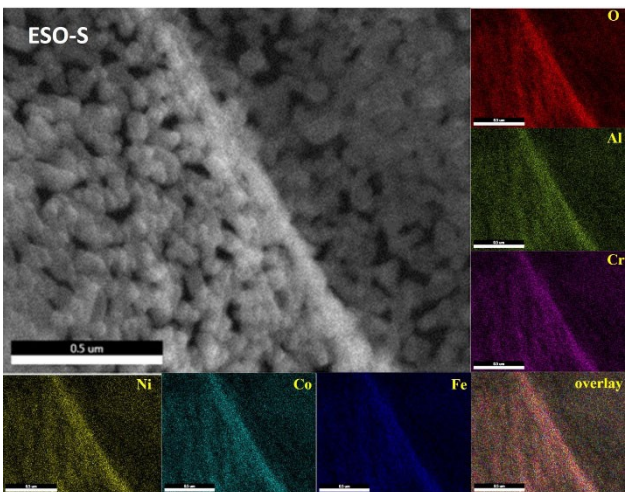


Figure 2. SEM and elemental composition mapping: Scanning electron microscope (SEM) image and elemental composition mapping of ESO-S showing all the constituting elements distributed homogeneously throughout the material (scale bars correspond to 0.5 μm)

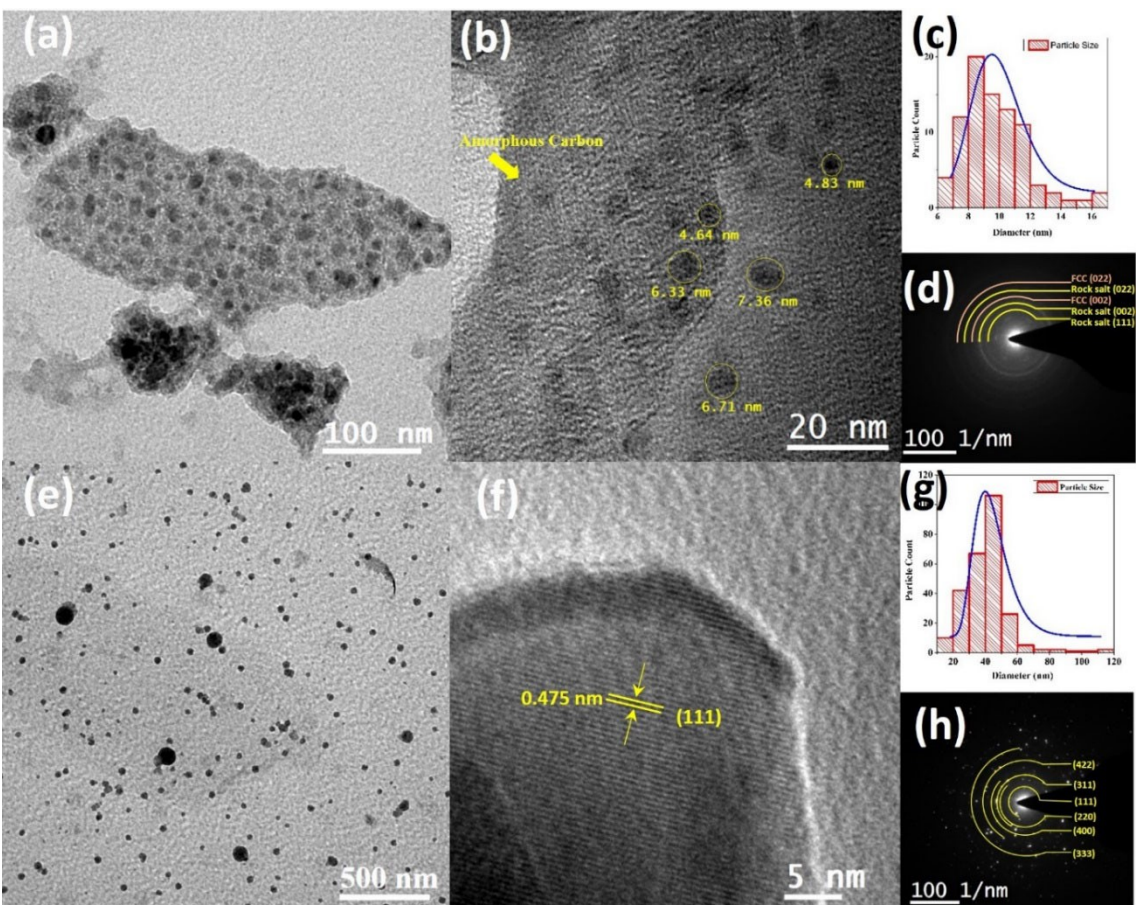


Figure 3. High-resolution transmission electron microscope (HRTEM) Analysis: HRTEM images showing the particle morphology and sizes of a, b) ESO-A and e) ESO-S, the particle size distribution of c) ESO-A and g) ESO-S. Selected area electron diffraction patterns of d) ESO-A and h) ESO-S.

the size distribution is estimated by a lognormal distribution. The average particles size is calculated to be ~9 nm. Selected area electron diffraction (SAED) patterns of ESO-A show characteristic ring patterns observed for nanocrystalline materials (Figure 3d). The diffraction ring patterns are in good agreement with XRD patterns of ESO-A and can be indexed to rock salt oxide and FCC alloy phases.

The HRTEM images of ESO-S in Figure 3(e) display nanocrystallites of sizes ranging from 20 nm to 120 nm. A high magnification image of an ESO-S particle is shown in Figure 3(f). Particle surface shows crystalline nature with few surface defects. No amorphous carbon traces are found. The interplanar spacing of the observed lattice fringes is calculated to be 0.475 nm, which corresponds to the (111) plane of the spinel phase. Size distribution of both ESO-S particles is shown in Figure 3(g). The average particle size is found to be ~40 nm. SAED patterns displayed in Figure 3(h) show the polycrystalline nature of the ESO-S. Several spots constituting to form rings in the SAED pattern show higher crystallinity in ESO-S when compared to ESO-A. The different ring patterns are in good agreement with that of the XRD pattern and are indexed to the corresponding miller planes of the spinel phase.

Surface characterization: X-ray photoelectron spectra (XPS) ESO-S and ESO-A samples are taken to confirm Ni, Co, Fe, Al, and O elements and analyze their surface oxidation states. Figure 4 represents the high-resolution spectra for Ni 2p, Co 2p, Fe 2p, Cr 2p, Al 2p, and O 1s regions for ESO-S and ESO-A. Analysis of M 2p_{3/2} and M 2p_{1/2} doublets observed in the 2p region of transition metals (M=Cr, Fe, Co, Ni) is carried out by following the method of Biesinger et al.^[60] M 2p_{3/2} regions are

deconvoluted into one or two sets of peaks, corresponding to the oxidation state of the transition metal. Each peak set consists of Gupta and Sen multiplets and shake-up related satellite peaks of the corresponding oxidation state. Since low energy M 2p_{1/2} regions give no new information, they are not considered in the peak analysis. Even though quantitative analysis of the bulk oxidation states is not possible, qualitative information about the surface oxidation states, which play a significant role in electrocatalysis, is acquired from XPS.

The Ni 2p_{3/2} peak is fitted with two sets of peaks corresponding to Ni³⁺ and Ni²⁺ species, as shown in Figure 4(a). As a starting point for the fit, Ni²⁺ and Ni³⁺ peak sets reported by Biesinger et al.^[61] for the NiOOH samples are taken as reference. While the peak area and FWHM ratios were constrained, the binding energies of the leading peaks of the two sets were unconstrained for the fitting to account for the chemical shifts. The fitting parameters are given in Table S2. The fitted peaks agree with the reported literature and indicate the presence of both Ni³⁺ and Ni²⁺ species on the sample surface. The final Ni²⁺ peak parameters closely resemble that of NiO spectra, validating the fitting methods. The relative amounts of Ni²⁺ and Ni³⁺ are approximately 1:3 (24.97% of Ni²⁺ and 75.03% of Ni³⁺). For comparison, a similar set of peaks are considered for the high-resolution Ni 2p_{3/2} spectrum of ESO-A. The surface Ni²⁺/Ni³⁺ ratio in ESO-A was approximately 2:1 (63.52% of Ni²⁺ and 36.48% of Ni³⁺). A large portion of Ni²⁺ is oxidized to the Ni³⁺ state during the spinel phase stabilization.

Similarly, Co 2p_{3/2} spectra of ESO-S are fitted with two sets of peaks, as shown in Figure 4(b). Here, spectra from CoO and

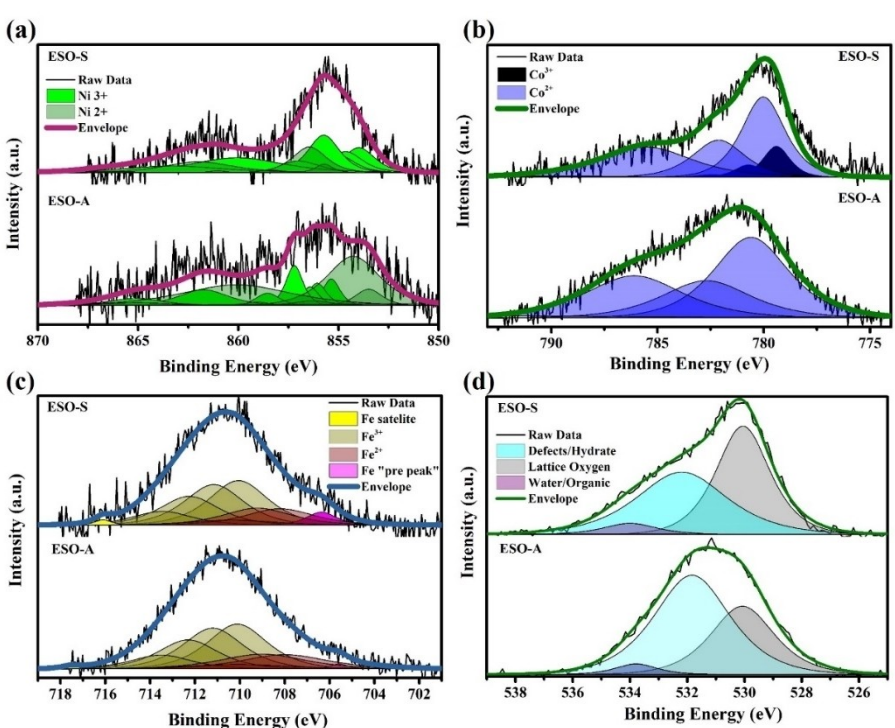


Figure 4. X-ray Photoelectron spectrum (XPS) comparison of a) Ni 2p, b) Co 2p, c) Fe 2p and d) O 1s surface states of ESO-S and ESO-A along with deconvoluted peaks.

CoOOH are taken as starting references for Co^{2+} and Co^{3+} states.^[60] Here, Co^{3+} contributes to 14.3% of the peak area, and Co^{2+} accounts for 85.7%. No trace of Co^{3+} is observed in the ESO-A sample and is fitted with the Co^{2+} set alone. The majority of the Ni^{2+} and Co^{2+} ions in ESO-A is in accordance with the XRD and Raman observations that the ESO-A has a rock salt phase with cations in M^{2+} oxidation state. Fe 2p_{3/2} region is fitted by considering Fe^{3+} and Fe^{2+} references from Fe_3O_4 samples reported by Grosvenor et al.^[62] Along with Fe^{2+} and Fe^{3+} multiplets, the Fe 2p3/2 spectrum is characterized by a pre-peak and a satellite for Fe^{2+} . Figure 4(c) shows Fe also exhibits the presence of both Fe^{2+} and Fe^{3+} in an approximate ratio of 1:3 (26.2% of Fe^{2+} and 77.8 of Fe^{3+}). Chromium 2p3/2 region is fitted with a single set of peaks corresponding to the Cr^{2+} state for ESO-A and ESO-S (Figure S4). The fitted peaks agree with those reported in the literature.^[60]

The oxygen 1 s spectrum of ESO-A and ESO-S are shown in Figure 4(d). The oxygen 1 s spectra can be resolved into three peaks corresponding to the contributions from the lattice, surface defects/hydrates, and organic contaminants, respectively. The major contributor to the spectrum in the case of ESO-S is the lattice oxygen. In contrast, the contribution from defects/hydrates is more in ESO-A due to the presence of amorphous carbon and the smaller crystallite size of the material. An increase in the lattice oxygen component also indicates the removal of the surface carbon layer present in the ESO-A.

Electrochemical performance

The electrochemical performance of $\text{Li}-\text{O}_2$ cells with ESO-A and spinel phased ESO-S as cathode reaction promoters is shown in Figure 5. 100 μL of 1 M LiTFSI in TEGDME electrolyte with 0.1 M LiI RM is used as electrolyte and a mass loading of 1 mg cm^{-2} (active material + conductive carbon) is maintained in all the cells. The cells are cycled with a current density of 0.25 mA cm^{-2} and the depth of discharge is limited to 1 mAh cm^{-2} . The corresponding specific capacity is 1000 mAh g^{-1} (considering only the active material and conductive carbon masses). Normalization of capacity with the electrode area (1.33 cm^2) is chosen instead of the mass loading as the latter sometimes leads to ambiguous capacity metrics and comparisons.^[63,64] The major reason for this ambiguity is the low mass loading (in hundreds of micrograms), which reduces the total cell current leading to an "apparent" stable electrochemical system as demonstrated by Noked et al.^[63] Furthermore, the effectiveness of the promoter is valid when the capacity is high.

The voltage profiles of cells with ESO-S and ESO-A are as shown in Figure 5(a). Despite the larger crystallite size compared to that of the as-prepared sample, the $\text{Li}-\text{O}_2$ cell with ESO-S performs 46 charge-discharge cycles before the capacity reduces to 60% of its initial value. The performance of ESO-A, with 35 cycles, seems to be comparable to that of ESO-S, but the discharge voltage drops below 2.5 V right from the 15th cycle. The terminal voltage vs. cycle number plot in

Figure 5(b) compares the stability of both cells. The ESO-S cell provides a stable voltage profile. In contrast, fluctuations in the terminal charge and discharge voltages are observed in an ESO-A cell, suggesting the superiority of spinel ESO-S over ESO-A.

The cyclic voltammograms of the $\text{Li}-\text{O}_2$ cells with ESO-S and ESO-A are shown in Figure 5(c). The cathodic scan in both cells shows a single peak corresponding to the oxygen reduction to form superoxide. The superoxide combines with a Li^+ ion to form lithium oxide, which further disproportionates to form Li_2O_2 . Peaks around 3.2 V, 3.5 V, 3.7 V vs. Li^+/Li are visible in the anodic scan, which corresponds to various steps of Li_2O_2 oxidation. Both anodic and cathodic currents of ESO-A cells are slightly higher than that of ESO-S, while the on-set potentials in anodic and cathodic directions are the same for both. The RM effects can also contribute to the low voltage peaks. I_3^-/I^- and I_2/I_3^- redox couples can have peaks around 3.0 and 3.2 V vs. Li^+/Li respectively. Both of these redox couples assist the oxidation of Li_2O_2 and hence contribute to the cells' cyclic stability. However, such phenomena are valid at low overpotentials, low current rates, and solvated Li_2O_2 species. At high overpotentials, solid Li_2O_2 oxidation on the surface of the reaction promoter proceeds, as discussed earlier. The depth of discharge of 1 mAh cm^{-2} is chosen such that contributions of the I_3^-/I^- and I_2/I_3^- redox couples of LiI RM and the ESO solid promoters can both be decoupled.

Different charge-discharge cycles of the ESO-S and ESO-A are shown in Figure 5(d) and (e), respectively. The charge and discharge plateau voltages match with the cyclic voltammetry peaks. ESO-A seems to have lower charging overpotentials when compared to ESO-S in the initial cycles but becomes unstable as cycling proceeds. ESO-S, on the other hand, delivers stable performance.

Post-cycling analysis

In order to understand the charge-discharge and failure mechanisms, the morphology of the cathode at various charge/discharge conditions is analyzed using SEM. Figure 6 shows the morphology evolution of the cathode with ESO-S as promoter during a 1 mAh cm^{-2} discharge-recharge cycle. Thin platelet-like products start appearing on the surface of the cathode and get denser upon continuous discharge. These products start disappearing during the recharging process, as seen in Figure 6. An increase and decrease in cell impedance (Figure S5) during the discharge and recharge process, respectively, also indicate the reversible Li_2O_2 formation/decomposition.

Along with the desired Li_2O_2 , several irreversible discharge products accumulate over the electrode surface, causing an increase in the charge/discharge overpotential. Figures 7(a) and S6 show the cycle performance of ESO-A and ESO-S cells at a high current density of 0.5 mA cm^{-2} , with capacity limited to 0.5 mAh cm^{-2} . The performance of ESO-A drastically reduces within the first few cycles, whereas ESO-S provides better stability. The formation of irreversible discharge products at this high current rate on both ESO-A and ESO-S electrodes is

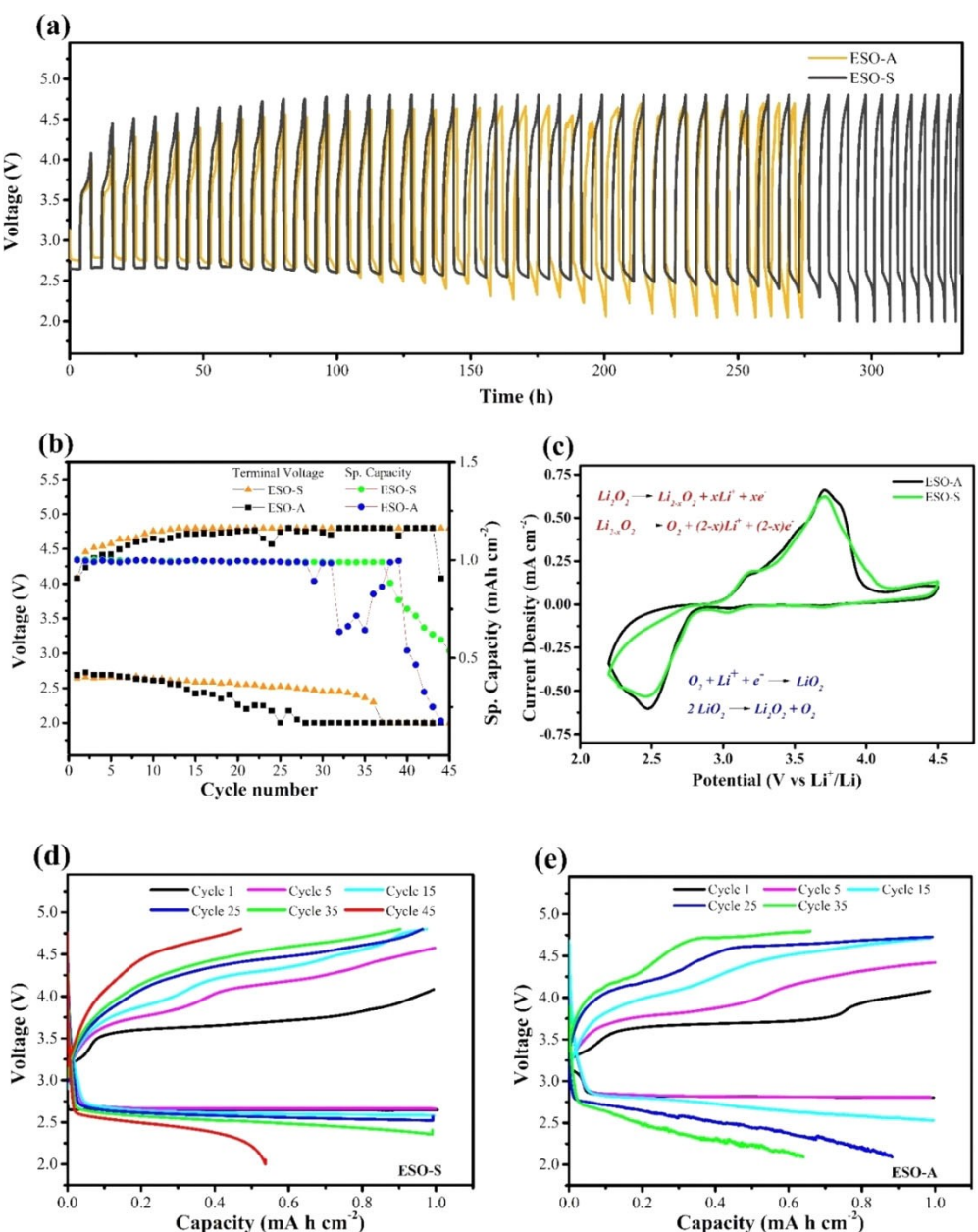


Figure 5. Electrochemical performance comparison of ESO-A and ESO-S: a) Voltage vs. time plot, b) terminal voltage, capacity vs. cycle number plot, and c) cyclic voltammetry comparison of ESO-A and ESO-S. Voltage vs. capacity plots at various cycles of d) ESO-S and e) ESO-A.

evident from the SEM images of the cycled electrodes (Figure 7b and c). Energy-dispersive X-ray spectra of the electrodes (Figure S7) indicate the presence of electrolyte components such as sulfur and iodine in addition to carbon and transition metals, indicating the formation of irreversible discharge product occurring due to the electrolyte degradation and RM side-reactions.^[65] However, the irreversible discharge products are more prominent in ESO-A when compared to ESO-S. The smaller particle size of ESO-A could enhance the formation of reactive oxygen species and hence induce high discharge product formation.

ESO-A shows higher discharge capacity when a full discharge test is carried out without any capacity limits, as

shown in Figure S8(a). However, the cell impedance after full discharge is very high for ESO-A (Figure S8b). This further shows that ESO-A is more prone to side reactions. The SEM images of the fully discharged electrodes show that the flake-like morphology is maintained in ESO-S whereas, in ESO-A, discharge products form a film on the surface of the electrode, completely blocking the mass transfer as shown in Figure S8(c and d).

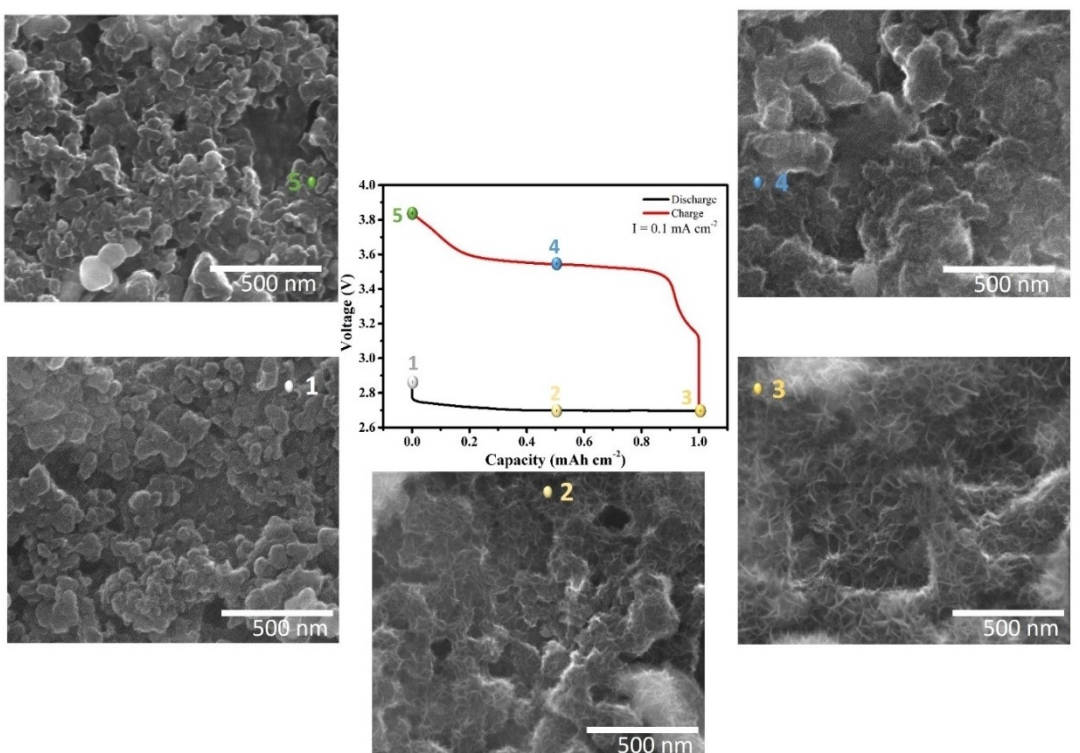


Figure 6. Morphology evolution of ESO-S cathode surface: 1) Blank electrode, 2) discharged up to 0.5 mAh cm^{-2} , 3) discharged up to 1 mAh cm^{-2} , 4) recharged up to 0.5 mAh cm^{-2} , and 5) recharged fully back up to 1 mAh cm^{-2} .

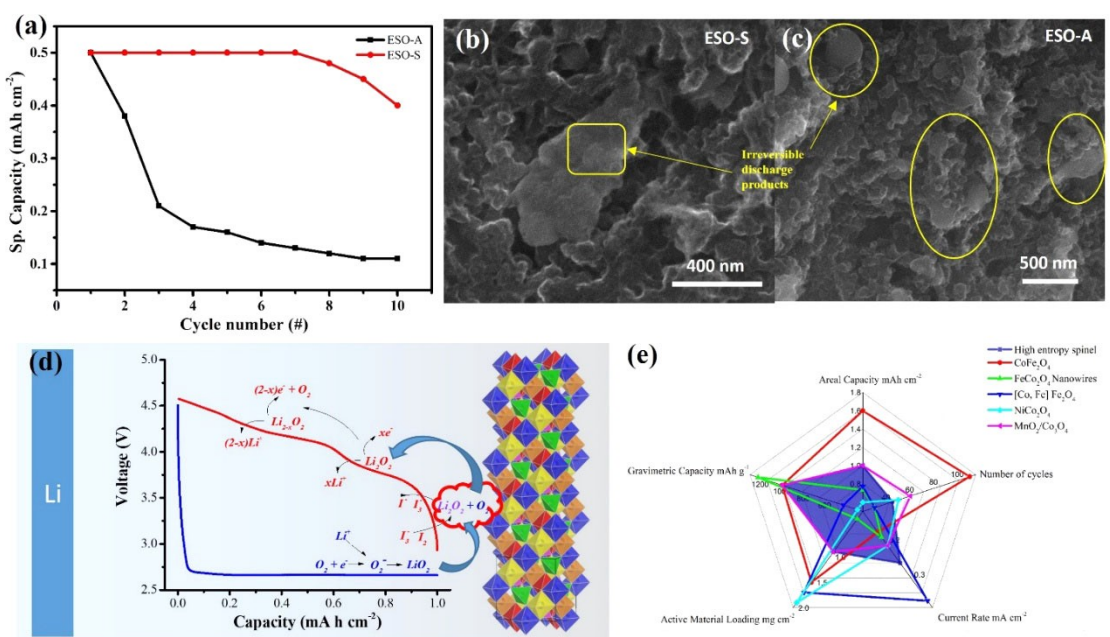


Figure 7. a) Capacity vs. cycle number plot for ESO-A and ESO-S cells at a current density of 0.5 mA cm^{-2} with capacity limited to 0.5 mAh cm^{-2} . SEM images of the electrodes after 10 cycles for b) ESO-S and c) ESO-A. d) Schematic of the charge/discharge mechanism and e) comparison of ESO-S cell performance with other spinel structured materials reported in the literature.

Discussion

A schematic of the reactions during charging and discharging is provided in Figure 7(d). In low ionicity solvents such as

TEGDME, the Li_2O_2 oxidation process involves multiple stages where lithium deficient intermediates are formed before it is completely oxidized. Amorphous and small crystallites Li_2O_2 are oxidized at low potentials. Li_2O_2 is oxidized to form sub-

stoichiometric intermediates like $\text{Li}_{2-x}\text{O}_2$, which further gets fully oxidized at higher overpotentials. The role of the reaction promoter in a $\text{Li}-\text{O}_2$ cell is to reduce this charging overpotential.

The surface electronic structure and defects of a promoter in close proximity to the reaction intermediate can enhance its surface electronic and ionic transport. Therefore, this solid-state activation by the promoter can facilitate the discharge product oxidation at low overpotentials. Furthermore, the dissolution of some of the transition metal (TM) cations in the electrolyte can lead to the formation of a TM doped discharge product, with increased conductivity.^[50,66–69]

Both entropy-stabilized oxides in the discussion have multiple cations in different surface oxidation states. The homogeneous mixing of the cations results in local disorder, and the presence of surface defects can be observed, as discussed in the previous sections. However, ESO-A has a smaller particle size, higher surface area when compared to ESO-S, and is embedded in an amorphous carbon matrix.

By virtue of their large surface area, smaller crystals provide more catalytic centers and outperform their larger counterparts in electrocatalysis. However, the high electrochemical activity materials are usually not selective towards Li_2O_2 formation alone in $\text{Li}-\text{O}_2$ batteries. They promote several other side reactions owing to the formation of O_2^- . The reactive oxygen species attacks and degrade other cell components such as a binder, electrolyte, and conductive carbon.^[70,71] The same can be seen in the case of ESO-A. ESO-A show higher capacity during full discharge than ESO-S, but the impedance of the cell increases. The irreversible reaction products block the Li_2O_2 -promoter contact and hence increase the overpotentials and drastically decrease the capacity retention in the following cycles, as seen in the electrochemical tests. On the other hand, ESO-S provides comparably stable cycles where the formation of irreversible discharge products is decreased. Furthermore, favorable structural modifications caused by different cations in octahedral and tetrahedral positions in the spinel ESO-S can make it a better promoter than ESO-A.^[72]

To put the ESOs performance in perspective of other reported spinel class promoters, a comparison of the ESO-S cell performance with the other spinel phase materials available in the literature is shown in Figure 7(e). Often comparison of different materials is made based on the gravimetric capacity and number of cycles in literature. For a judicious comparison, we consider five important parameters that can drastically affect cell performance: active material loading, areal capacity, gravimetric capacity, number of cycles, and current drawn per area. As can be seen from the radar plot, current rate and active material loading can have severe implications on the cell performance (only those reports with active material loading greater than 1 mg cm^{-2} and current rates greater than 0.15 mA cm^{-2} are considered for the comparison). Entropy stabilized oxides, with comparatively low cobalt and nickel content and in the absence of any specialized and complicated morphological features, perform comparably to other spinels. A detailed comparison table is provided in Supplementary Table S3.

Conclusion

In summary, two entropy-stabilized-nanocrystalline materials, ESO-A and ESO-S, are synthesized in a simple and scalable method. ESO-A prepared from a sol-gel combustion method is found to have a mixed rock-salt-FCC alloy phase embedded in an amorphous carbon matrix. Thermal treatment of ESO-A in air leads to the formation of a phase pure entropy stabilized spinel ESO-S. Both the materials have spheroidal morphology. The surface oxidation states and chemical homogeneity of the cations are analyzed. Both materials are applied as cathode reaction promoters in $\text{Li}-\text{O}_2$ batteries for the first time. Cells were tested at 0.25 mA cm^{-2} current density with a capacity of 1 mAh cm^{-2} . Spinel phased ESO-S is found to provide superior performance when compared to ESO-A. The morphologies of the discharge products and cell failure are analysed using ex-situ SEM analysis. Local structural modifications due to the presence of dissimilar cations in octahedral and tetrahedral sites and surface defects are believed to be the reason for the promoter performance.

The entropy stabilized oxide brings excellent flexibility in modulating the structure, both at surface and bulk scale. The compositional and morphological variations of the materials can be further explored in $\text{Li}-\text{O}_2$ batteries and other functional applications. The fundamental understanding of the migration of cations from octahedral to tetrahedral positions can provide further insights in the entropy stabilized material design and property optimization.

Experimental Section

Material synthesis

Entropy stabilized oxide is prepared by a sol-gel combustion method. In a typical synthesis, 1 mM each of analytical grade $\text{Co}(\text{NO}_3)_2 \cdot 6\text{H}_2\text{O}$, $\text{Cr}(\text{NO}_3)_3 \cdot 9\text{H}_2\text{O}$, $\text{Ni}(\text{NO}_3)_2 \cdot 6\text{H}_2\text{O}$, $\text{Al}(\text{NO}_3)_3 \cdot 9\text{H}_2\text{O}$, $\text{Fe}(\text{NO}_3)_3 \cdot 9\text{H}_2\text{O}$ metal nitrate precursors are taken and dissolved in 200 mL of Millipore water. 5 mM of citric acid is added, and the solution is agitated thoroughly using magnetic stirring. The pH of the solution was adjusted to 7 by adding ammonia. The final sol is annealed at 100°C for 24 h to get dried gel. The dried gels were collected and charged in a tubular furnace and were subjected to combustion reaction at 300°C . The combustion reaction is carried out in a flowing Ar gas atmosphere for 1 h. Once the furnace naturally cools down, samples are collected, milled thoroughly using mortar and pestle, and stored for further studies. The collected “as-prepared entropy stabilized oxide” sample is abbreviated as ESO-A in this manuscript. A known amount of ESO-A sample is subjected to heat treatment at 900°C . The heating rate is maintained at 5°C min^{-1} , and the sample is soaked at 900°C for 9 hours to prepare spinel entropy stabilized oxide ESO-S.

Physical characterization

X-ray diffraction (XRD) measurements of the samples were carried out using a Rigaku Smartlab X-ray diffractometer with a Cu K_α ($\lambda = 1.5418 \text{ \AA}$) source. XRD patterns were recorded with a step size of $0.02^\circ 2\theta$ and a scan rate of $2.5^\circ \text{ min}^{-1}$. Rietveld refinement of the XRD patterns was carried out using GSAS II software. Raman spectra of the samples were recorded using Horiba Labram Raman

Spectrometer. Scanning electron microscope (SEM) images and elemental composition mapping along with energy dispersive spectroscopy were taken using Quanta 200 (FEG) with EDAX attachment. Surface oxidation states were analyzed using X-ray photoelectron spectroscopy (XPS), with Mg K_{α} X-ray source, PHOIBOS 100MCD from SPECS analyzer operated at ultra-high vacuum (10^{-9} mbar). XPS peaks were fitted using CASA XPS software. A Shirley-type background was chosen, and GL (70) peak shape function was used to deconvolute the XPS spectra. Thermogravimetric analysis was carried out in SDTQ600 TGA analyzer by TA instruments. The temperature was ramped from room temperature to 1000°C at a $10^{\circ}\text{C min}^{-1}$ rate in an air atmosphere (150 mL min^{-1}). The specific surface area of the samples was measured via a nitrogen adsorption/desorption isotherm at liquid nitrogen temperatures (77 K) by Micrometrics ASAP 2020 surface area and porosity analyzer.

Electrochemical characterization

$\text{Li}-\text{O}_2$ cells were tested with the synthesized materials as cathode reaction promoters. Cell cathode was prepared by coating active materials on a gas diffusion electrode made using carbon cloth (Torey). Active material, a conductive carbon (Acetylene black), and a binder polyvinylidene fluoride (PVDF) were taken in a 5:4:1 ratio and mixed thoroughly to get a homogenous mixture. This mixture was dispersed in N-methyl pyrrolidone to obtain a slurry, which was coated over the GDL coated carbon cloth current collector by a brush coating method. Mass loadings of active material + conductive carbon of $\sim 1 \text{ mg cm}^{-2}$ were maintained in all the coated electrodes. The brush-coated electrodes were dried in a vacuum oven at 80°C for at least 8 hours to remove all the solvents. After drying, the electrodes were subjected to hot press at 80°C for 1 hour to obtain a uniform coating. Finally, electrodes were cut into disks of 13 mm diameter and stored in an Ar-filled glove box to avoid moisture exposure. The electrolyte used was 1 M LiTFSI (Lithium bis(trifluoromethanesulfonyl)imide), and 0.1 M lithium iodide (LiI) salts in tetra ethylene glycol dimethyl ether (TEGDME). Electrolyte solvent TEGDME was dried on molecular sieves for at least 72 hours before preparation of the electrolyte to remove any moisture content. Salts, LiI, and LiTFSI were also dried in a vacuum oven at 100°C to remove any adsorbed moisture, and the electrolyte was prepared and stored in an Ar-filled glove box (MBraun) with oxygen and water contents less than 0.1 ppm. Lithium- O_2 cells were fabricated in a 2035-coin cell configuration in the glove box. The specialized 2032 cells for metal-air batteries, having holes at the positive side case, were used. A lithium disk of 13 mm diameter, a glass-fiber separator (Whatman GF/A) soaked in $100 \mu\text{L}$ electrolyte, and the prepared positive electrode are sandwiched in the 2032 coin cells to form the cells.

Coin cell testing was carried out in a leak-proof oxygen-filled chamber kept at 1 bar pressure. Before transferring the coin cells, the chamber was purged with oxygen to remove any moisture present. Galvanostatic charge/discharge (GCPL) and cyclic voltammetry studies were carried out using a Biologic BCS-310 battery cycler. GCPL measurements were carried out with a constant current of 0.25 mA cm^{-2} and a capacity limitation of 1 mAh cm^{-2} . Cyclic voltammetry was carried out between 2.2 V to 4.5 V vs. Li^+/Li with a scan rate of 0.1 mV s^{-1} .

Post-cycling analysis

Cells after cycling are cut open inside the glove box using a de-crimping tool. The cycled electrodes are washed in TEGDME solvent and are kept for drying in a vacuum. Samples for the analysis are prepared inside the glove box and transferred to the

scanning electron microscope in an airtight container to avoid contact with moisture.

Acknowledgements

Authors thank the Indian Institute of Technology, Madras, for financial support. One of the authors thanks the Department of Science and Technology (DST) for the financial support to establish Nano Functional Materials Technology Centre (NFMTC) through the SR/NM/NAT/02-2005 project.

Conflict of Interest

The authors declare no conflict of interest.

Data Availability Statement

Data sharing is not applicable to this article as no new data were created or analyzed in this study.

Keywords: energy conversion • entropy stabilized oxides • lithium- O_2 batteries • oxygen electrocatalysis • spinel phases

- [1] D. B. Miracle, O. N. Senkov, *Acta Mater.* **2017**, *122*, 448–511.
- [2] S. Ranganathan, *Curr. Sci.* **2003**, *85*, 1404–1406.
- [3] E. P. George, D. Raabe, R. O. Ritchie, *Nat. Rev. Mater.* **2019**, *4*, 515–534.
- [4] J.-W. Yeh, S.-K. Chen, S.-J. Lin, J.-Y. Gan, T.-S. Chin, T.-T. Shun, C.-H. Tsau, S.-Y. Chang, *Adv. Eng. Mater.* **2004**, *6*, 299–303.
- [5] C. M. Rost, E. Sachet, T. Borman, A. Mabalagh, E. C. Dickey, D. Hou, J. L. Jones, S. Curtarolo, J. P. Maria, *Nat. Commun.* **2015**, *6*, 1–8.
- [6] D. Bérardan, S. Franger, D. Dragoe, A. K. Meena, N. Dragoe, *Phys. Status Solidi RRL* **2016**, *10*, 328–333.
- [7] J. Wang, D. Stenzel, R. Azmi, S. Najib, K. Wang, J. Jeong, A. Sarkar, Q. Wang, P. A. Sukkurji, T. Bergfeldt, M. Botros, J. Maibach, H. Hahn, T. Brezesinski, B. Breitung, *Electrochim. Acta* **2020**, *1*, 60–74.
- [8] J. L. Braun, C. M. Rost, M. Lim, A. Giri, D. H. Olson, G. N. Kotsonis, G. Stan, D. W. Brenner, J. P. Maria, P. E. Hopkins, *Adv. Mater.* **2018**, *30*, 1–8.
- [9] Z. Grzesik, G. Smola, M. Stygar, J. Dąbrowa, M. Zajusz, K. Mroczka, M. Danielewski, *J. Eur. Ceram. Soc.* **2019**, *39*, 4292–4298.
- [10] D. Berardan, A. K. Meena, S. Franger, C. Herrero, N. Dragoe, *J. Alloys Compd.* **2017**, *704*, 693–700.
- [11] P. B. Meisenheimer, T. J. Kratofil, J. T. Heron, *Sci. Rep.* **2017**, *7*, 3–8.
- [12] M. P. Jimenez-Segura, T. Takayama, D. Bérardan, A. Hoser, M. Reehuis, H. Takagi, N. Dragoe, *Appl. Phys. Lett.* **2019**, *114*, 1–5.
- [13] J. Zhang, J. Yan, S. Calder, Q. Zheng, M. A. McGuire, D. L. Abernathy, Y. Ren, S. H. Lapidus, K. Page, H. Zheng, J. W. Freeland, J. D. Budai, R. P. Hermann, *Chem. Mater.* **2019**, *31*, 3705–3711.
- [14] X. Yan, L. Constantin, Y. Lu, J. F. Silvain, M. Nastasi, B. Cui, *J. Am. Ceram. Soc.* **2018**, *101*, 4486–4491.
- [15] J. Dąbrowa, M. Stygar, A. Mikula, A. Knapik, K. Mroczka, W. Tejchman, M. Danielewski, M. Martin, *Mater. Lett.* **2018**, *216*, 32–36.
- [16] S. Marik, D. Singh, B. Gonano, F. Veillon, D. Pelloquin, Y. Bréard, *Scr. Mater.* **2020**, *183*, 107–110.
- [17] Y. Sharma, B. L. Musico, X. Gao, C. Hua, A. F. May, A. Herklotz, A. Rastogi, D. Mandrus, J. Yan, H. N. Lee, M. F. Chisholm, V. Keppens, T. Z. Ward, *Phys. Rev. Mater.* **2018**, *2*, 1–6.
- [18] S. Jiang, T. Hu, J. Gild, N. Zhou, J. Nie, M. Qin, T. Harrington, K. Vecchio, J. Luo, *Scr. Mater.* **2018**, *142*, 116–120.
- [19] R. Witte, A. Sarkar, R. Kruk, B. Eggert, R. A. Brand, H. Wende, H. Hahn, *Phys. Rev. Mater.* **2019**, *3*, 1–9.
- [20] F. Okejiri, Z. Zhang, J. Liu, M. Liu, S. Yang, S. Dai, *ChemSusChem* **2020**, *13*, 111–115.

- [21] K. Ren, Q. Wang, G. Shao, X. Zhao, Y. Wang, *Scr. Mater.* **2020**, *178*, 382–386.
- [22] H. Qiao, X. Wang, Q. Dong, H. Zheng, G. Chen, M. Hong, C. P. Yang, M. Wu, K. He, L. Hu, *Nano Energy* **2021**, *86*, 106029.
- [23] W. Jiang, T. Wang, H. Chen, X. Suo, J. Liang, W. Zhu, H. Li, S. Dai, *Nano Energy* **2021**, *79*, 105464.
- [24] T. Jin, X. Sang, R. R. Unocic, R. T. Kinch, X. Liu, J. Hu, H. Liu, S. Dai, *Adv. Mater.* **2018**, *30*, 1707512.
- [25] J. Zhou, J. Zhang, F. Zhang, B. Niu, L. Lei, W. Wang, *Ceram. Int.* **2018**, *44*, 22014–22018.
- [26] F. Monteverde, F. Saraga, *J. Alloys Compd.* **2020**, *824*, 153930.
- [27] Y. Zhang, Z. Bin Jiang, S. K. Sun, W. M. Guo, Q. S. Chen, J. X. Qiu, K. Plucknett, H. T. Lin, *J. Eur. Ceram. Soc.* **2019**, *39*, 3920–3924.
- [28] J. Gild, Y. Zhang, T. Harrington, S. Jiang, T. Hu, M. C. Quinn, W. M. Mellor, N. Zhou, K. Vecchio, J. Luo, *Sci. Rep.* **2016**, *6*, 2–11.
- [29] Y. Qin, J. X. Liu, F. Li, X. Wei, H. Wu, G. J. Zhang, *J. Adv. Ceram.* **2019**, *8*, 148–152.
- [30] A. J. Wright, Q. Wang, C. Huang, A. Nieto, R. Chen, J. Luo, *J. Eur. Ceram. Soc.* **2020**, *40*, 2120–2129.
- [31] D. Bérardan, S. Franger, A. K. Meena, N. Dragoe, *J. Mater. Chem. A* **2016**, *4*, 9536–9541.
- [32] N. Osenciat, D. Bérardan, D. Dragoe, B. Léridon, S. Holé, A. K. Meena, S. Franger, N. Dragoe, *J. Am. Ceram. Soc.* **2019**, *102*, 6156–6162.
- [33] A. Sarkar, L. Velasco, D. Wang, Q. Wang, G. Talasila, L. de Biasi, C. Kübel, T. Brezesinski, S. S. Bhattacharya, H. Hahn, B. Breitung, *Nat. Commun.* **2018**, *9*, DOI 10.1038/s41467-018-05774-5.
- [34] Q. Wang, A. Sarkar, D. Wang, L. Velasco, R. Azmi, S. S. Bhattacharya, T. Bergfeldt, A. Düvel, P. Heijmans, T. Brezesinski, H. Hahn, B. Breitung, *Energy Environ. Sci.* **2019**, *12*, 2433–2442.
- [35] T.-Y. Chen, S.-Y. Wang, C.-H. Kuo, S.-C. Huang, M.-H. Lin, C.-H. Li, H.-Y. T. Chen, C.-C. Wang, Y.-F. Liao, C.-C. Lin, Y.-M. Chang, J.-W. Yeh, S.-J. Lin, T.-Y. Chen, H.-Y. Chen, *J. Mater. Chem. A* **2020**, *8*, 21756–21770.
- [36] T. X. Nguyen, J. Patra, J.-K. Chang, J.-M. Ting, *J. Mater. Chem. A* **2020**, *8*, 18963–18973.
- [37] Y. Zheng, Y. Yi, M. Fan, H. Liu, X. Li, R. Zhang, M. Li, Z.-A. Qiao, *Energy Storage Mater.* **2019**, *23*, 678–683.
- [38] L. Y. Tian, Z. Zhang, S. Liu, G. Li, X. P. Gao, *Energy Environ. Mater.* **2021**, eem2.12215.
- [39] T. X. Nguyen, Y. Liao, C. Lin, Y. Su, J. Ting, *Adv. Funct. Mater.* **2021**, *31*, 2101632.
- [40] Z. Jin, J. Lyu, Y.-L. Zhao, H. Li, Z. Chen, X. Lin, G. Xie, X. Liu, J.-J. Kai, H.-J. Qiu, *Chem. Mater.* **2021**, *33*, 1771–1780.
- [41] D. Wang, Z. Liu, S. Du, Y. Zhang, H. Li, Z. Xiao, W. Chen, R. Chen, Y. Wang, Y. Zou, S. Wang, *J. Mater. Chem. A* **2019**, *7*, 24211–24216.
- [42] T. Li, Y. Yao, B. H. Ko, Z. Huang, Q. Dong, J. Gao, W. Chen, J. Li, S. Li, X. Wang, R. Shahbazian-Yassar, F. Jiao, L. Hu, *Adv. Funct. Mater.* **2021**, *31*, 2010561.
- [43] N. Kumar Katiyar, K. Biswas, J.-W. Yeh, S. Sharma, C. Sekhar Tiwary, *Nano Energy* **2021**, *88*, 106261.
- [44] H. Chen, J. Fu, P. Zhang, H. Peng, C. W. Abney, K. Jie, X. Liu, M. Chi, S. Dai, *J. Mater. Chem. A* **2018**, *6*, 11129–11133.
- [45] D. Feng, Y. Dong, L. Zhang, X. Ge, W. Zhang, S. Dai, Z. Qiao, *Angew. Chem. Int. Ed.* **2020**, *59*, 19503–19509; *Angew. Chem.* **2020**, *132*, 19671–19677.
- [46] K. Gu, D. Wang, C. Xie, T. Wang, G. Huang, Y. Liu, Y. Zou, L. Tao, S. Wang, *Angew. Chem. Int. Ed.* **2021**, *60*, 20253–20258.
- [47] B. D. McCloskey, D. Addison, *ACS Catal.* **2017**, *7*, 772–778.
- [48] B. D. McCloskey, R. Scheffler, A. Speidel, D. S. Bethune, R. M. Shelby, A. C. Luntz, *J. Am. Chem. Soc.* **2011**, *133*, 18038–18041.
- [49] K. He, X. Bi, Y. Yuan, T. Foroozan, B. Song, K. Amine, J. Lu, R. Shahbazian-Yassar, *Nano Energy* **2018**, *49*, 338–345.
- [50] R. Black, J. H. Lee, B. Adams, C. A. Mims, L. F. Nazar, *Angew. Chem. Int. Ed.* **2013**, *52*, 392–396; *Angew. Chem.* **2013**, *125*, 410–414.
- [51] X. Gao, Y. Chen, L. R. Johnson, Z. P. Jovanov, P. G. Bruce, *Nat. Energy* **2017**, *2*, 1–7.
- [52] W. Zhang, Y. Shen, D. Sun, Z. Huang, J. Zhou, H. Yan, Y. Huang, *Nano Energy* **2016**, *30*, 43–51.
- [53] T. Zhang, K. Liao, P. He, H. Zhou, *Energy Environ. Sci.* **2016**, *9*, 1024–1030.
- [54] B. Niu, F. Zhang, H. Ping, N. Li, J. Zhou, L. Lei, J. Xie, J. Zhang, W. Wang, Z. Fu, *Sci. Rep.* **2017**, *7*, 3421.
- [55] B. Rivas-Murias, V. Salgueirido, *J. Raman Spectrosc.* **2017**, *48*, 837–841.
- [56] S. H. Ng, J. Wang, D. Wexler, S. Y. Chew, H. K. Liu, *J. Phys. Chem. C* **2007**, *111*, 11131–11138.
- [57] A. Sarkar, B. Eggert, R. Witte, J. Lill, L. Velasco, Q. Wang, J. Sonar, K. Ollefs, S. S. Bhattacharya, R. A. Brand, H. Wende, F. M. F. de Groot, O. Clemens, H. Hahn, R. Kruck, *Acta Mater.* **2022**, *226*, 117581.
- [58] W. Wang, Z. Ding, X. Zhao, S. Wu, F. Li, M. Yue, J. P. Liu, *J. Appl. Phys.* **2015**, *117*, 1–5.
- [59] Z. Ž. Lazarević, Č. Jovalekić, A. Milutinović, D. Sekulić, V. N. Ivanovski, A. Rečnik, B. Cekić, N. Ž. Romčević, *J. Appl. Phys.* **2013**, *113*, 187221.
- [60] M. C. Biesinger, B. P. Payne, A. P. Grosvenor, L. W. M. Lau, A. R. Gerson, R. S. C. Smart, *Appl. Surf. Sci.* **2011**, *257*, 2717–2730.
- [61] M. C. Biesinger, B. P. Payne, L. W. M. Lau, A. Gerson, R. S. C. Smart, *Surf. Interface Anal.* **2009**, *41*, 324–332.
- [62] A. P. Grosvenor, B. A. Kobe, M. C. Biesinger, N. S. McIntyre, *Surf. Interface Anal.* **2004**, *36*, 1564–1574.
- [63] M. Noked, M. A. Schroeder, A. J. Pearse, G. W. Rubloff, S. B. Lee, *J. Phys. Chem. Lett.* **2016**, *7*, 211–215.
- [64] J. Jiang, H. Deng, X. Li, S. Tong, P. He, H. Zhou, *ACS Appl. Mater. Interfaces* **2016**, *8*, 10375–10382.
- [65] G. Leverick, M. Tułodziecki, R. Tatara, F. Bardé, Y. Shao-Horn, *Joule* **2019**, *3*, 1106–1126.
- [66] Y. Wang, N.-C. Lai, Y.-R. Lu, Y. Zhou, C.-L. Dong, Y.-C. Lu, *Joule* **2018**, *2*, 2364–2380.
- [67] S. Ganapathy, B. D. Adams, G. Stenou, M. S. Anastasaki, K. Goubitz, X. Miao, L. F. Nazar, M. Wagemaker, *J. Am. Chem. Soc.* **2014**, *136*, 16335–16344.
- [68] M. D. Radin, C. W. Monroe, D. J. Siegel, *Chem. Mater.* **2015**, *27*, 839–847.
- [69] K. P. C. Yao, M. Risch, S. Y. Sayed, Y. L. Lee, J. R. Harding, A. Grimaud, N. Pour, Z. Xu, J. Zhou, A. Mansour, F. Bardé, Y. Shao-Horn, *Energy Environ. Sci.* **2015**, *8*, 2417–2426.
- [70] G. Karkera, A. S. Prakash, *ACS Appl. Mater. Interfaces* **2019**, *11*, 27870–27881.
- [71] R. A. Wong, C. Yang, A. Dutta, O. Minho, M. Hong, M. L. Thomas, K. Yamanaka, T. Ohta, K. Waki, H. R. Byon, *ACS Energy Lett.* **2018**, *3*, 592–597.
- [72] Q. Huang, B. He, W. Zhang, J. Wang, Y. Fan, X. Mai, Y. Wang, Y. Hou, Y. Du, P. Xie, F. Dang, *ACS Appl. Mater. Interfaces* **2020**, *12*, 30268–30279.

Manuscript received: February 7, 2022

Revised manuscript received: February 23, 2022

Accepted manuscript online: February 23, 2022

Version of record online: March 16, 2022